Domain walls and defects in ferroelectric inorganic halide perovskites $CsGeX_3$ (X = Cl, Br, I)

Kristoffer Eggestad, Benjamin A. D. Williamson, and Sverre M. Selbach*
Department of Materials Science and Engineering, NTNU - Norwegian University of Science and Technology, NO-7491 Trondheim, Norway

(Received 11 November 2025; accepted 8 May 2026; published 1 June 2026)

Among all-inorganic halide perovskites, the only known ferroelectrics are the family of $CsGeX_3$ (X = Cl, Br, I). Here, we study their ferroelectric domain walls (DWs) and common point defects by density functional theory (DFT) calculations and investigate the interplay between DWs and defects. The most stable defects are V_X and V_{Cs} and the former shows low migration barriers and high mobility. In contrast to oxide ferroelectrics, the affinity between point defects and DWs is negligible, reflecting the subtle structural distortions at $CsGeX_3$ DWs. Concomitantly, the formation energies and migration energy barriers of $CsGeX_3$ DWs are small compared to oxides, and neither V_X nor V_{Cs} pin migrating DWs. The band-gap invariance across DWs and the lack of affinity towards intrinsic charged-point defects imply that conducting DWs for nanoelectronics may be challenging to realize in $CsGeX_3$. However, shallow *p*-type defect levels and low-hole effective masses suggest that high *p*-type conductivity may be achievable in nominally ferroelectric $CsGeX_3$. The low DW migration energy barriers and insignificant DW pinning by point defects make $CsGeX_3$ promising materials as robust soft ferroelectrics for high-frequency switching applications with low energy dissipation.

DOI: 10.1103/bf5v-24b2

I. INTRODUCTION

Halide perovskites have been mostly studied for their optoelectronic and photovoltaic properties [1–4]. Among these, there are also ferroelectric candidates [5,6], such as the hybrid organic-inorganic compounds with an organic A cation, e.g. MAPI ($CH_3NH_3PbI_3$) [7–9]. Among ferroelectric halide perovskites, the family of $CsGeX_3$ (X = Cl, Br, I) are the only known all-inorganic compounds [10,11]. The structural ground state is rhombohedral *R*3*m*, making them isostructural with prototypical perovskite oxides $BaTiO_3$ and $KNbO_3$ [12–17], and different from MAPI which is typically reported as tetragonal at room temperature [18]. They possess T_C s of 155°C, 238°C, and 277°C for X = Cl, Br, I [19], respectively, and polarizations [10] within $10 - 20\ \mu C/cm^2$. Most studies hitherto of $CsGeX_3$ have emphasized photovoltaic properties, including several *ab initio* studies of the electronic structure [20–25]. $CsGeCl_3$ has also shown promise as a *p*-type conductor, similar to Sn(II)O, where traditionally localized deep lying holes situated on O 2*p* (in $Sn(IV)O_2$, an *n*-type conductor) are now delocalized thanks to covalency between anion *p* and Ge 4*s*, lowering the effective mass of holes and the ionization potential allowing for low formation energy shallow defects, such as V_{Cs} [26,27]. The related $CsSnX_3$ and $CsPbX_3$ also possess B-site lone pairs, but here tensile strain is needed to stabilize polarization [28].

Conductive ferroelectric DWs were first reported in La-doped $BiFeO_3$ [29], but have later been shown in a multitude of materials systems [30–32]. DWs in ferroelectric and ferroelastic oxides are known to become conducting [30,33] from either intrinsic effects, such as band bending at neutral or charged DWs [29,32,34,35], or by extrinsic effects, such as electronic charge compensation of charged point defects accumulating at the DWs [36–38]. The space group of $CsGeX_3$, *R*3*m*, allows 71°, 109°, and 180° ferroelectric DWs. The 71° and 109° DWs must also be ferroelastic as the strain state changes across these walls. Our study of DWs in $CsGeX_3$ is also motivated by the high charge carrier mobility [39,40], defect tolerance [40–44], and intermediate band semiconductivity [20,45], all implying that different physical DW properties compared to oxides are anticipated.

Here, we use density functional theory (DFT) calculations to study DWs and point defects in ferroelectric $CsGeX_3$ (X = Cl, Br, I). We calculate electronic structure, DW mobility, point defect formation energies and migration barriers, and interactions between DWs and point defects. $CsGeX_3$ exhibit significantly different DW energies, mobilities, and electronic structures compared to corresponding oxides. High DW mobility, point defect insensitivity, and propensity to *p*-type doping give the all-inorganic halide perovskites a distinctly complementary technological potential compared to oxide ferroelectrics.

II. COMPUTATIONAL DETAILS

Point defects and DWs in $CsGeX_3$ have been investigated using density functional theory (DFT) within the `VASP` code [46–48]. Interactions between core and valence electrons [Cs: ($4s^2$, $4p^6$, $5s^1$), Ge: ($3d^{10}$, $4s^2$, $4p^2$), Cl: ($3s^2$, $3p^5$), Br: ($4s^2$, $4p^5$), I: ($5s^2$, $5p^5$)] were treated using

*Contact author: selbach@ntnu.no

Published by the American Physical Society under the terms of the Creative Commons Attribution 4.0 International license. Further distribution of this work must maintain attribution to the author(s) and the published article's title, journal citation, and DOI.

TABLE I. Calculated and experimental lattice parameters and Ge-X bond lengths for the primitive unit cell of $CsGeCl_3$, $CsGeBr_3$ and $CsGeI_3$. The bonds described are the bonds shown in Fig. 1.

		PBE	PBEsol	HSE06	Expt.
$CsGeCl_3$	a,b,c (Å)	5.519	5.294	5.513	5.444 [11], 5.434 [19], 5.391 [65]
	α, β, γ (deg)	89.00	89.76	89.49	89.63 [11], 89.72 [19], 89.71 [65]
	Ge-Cl (Å)	2.41	2.42	2.37	2.35 [19]
$CsGeBr_3$	a,b,c (Å)	5.744	5.504	5.731	5.636 [19,64], 5.638 [65]
	α, β, γ (deg)	88.45	89.53	88.46	88.74 [19,64], 88.73 [65]
	Ge-Br (Å)	2.58	2.60	2.54	2.53 [19]
$CsGeI_3$	a,b,c (Å)	6.108	5.860	6.081	5.983 [19]
	α, β, γ (deg)	88.25	89.49	88.14	88.61 [19]
	Ge-I (Å)	2.79	2.80	2.75	2.75 [19]

the projector-augmented-wave method (PAW) [49,50]. The HSE06 functional [51] (Heyd-Scuseria-Ernzerhof screened hybrid functional, with mixing parameter $\alpha = 0.25$ and screening parameter $\omega = 0.11$ bohr^{-1}) was used for all bulk structure calculations, as it yields lattice parameters in close agreement with experimental values (see Table I) and is known to provide accurate descriptions of electronic structure and carrier localization [52,53]. Due to the high computational cost of HSE06, the PBEsol [54] functional (Perdew-Burke-Ernzerhof revised for solids) was used to investigate defect mobilities and domain walls. A plane-wave energy cutoff of 400 eV was used for all calculations. The effects of spin-orbit coupling (SOC) were studied for all three halide systems, however, only minor changes in the electronic structure of $CsGeI_3$ were observed (see Supplemental Material (SM) [55] Fig. S5), and, thus, SOC was omitted in subsequent calculations to reduce computational cost.

Electronic density of states (DOS) were calculated using primitive cells containing 5 atoms. Geometries and atomic positions were optimised until all forces on all ions were less than 1×10^{-4} eV Å^{-1} using $8 \times 8 \times 8$ Γ-centred k-point meshes. k-points along high-symmetry paths, for electronic band structure calculations, were generated using the `SUMO` program [56].

Polarization was estimated using the point charge model, with formal charges (FC) and Born effective charges (BEC), and the Berry phase method. BEC were calculated using finite differences and tabulated in SM [55] Table S6. The finite differences method also gives dielectric, piezoelectric and elastic tensors, presented in SM [55] Tables S7, S8, and S9. Similar properties have been estimated using density functional perturbation theory (DFPT) with the PBEsol functional and are displayed in SM [55] Tables S11, S12, S13, and S14. Intrinsic point defect formation energies were calculated using [57]

$$\Delta H_F(D,q) = E_D(q) - E_H + \sum_i n_i(E_i + \mu_i) + q\left(E_F + E_{vbm} + E_{corr}^{pot}\right) + E_{corr}^{IC} + E_{corr}^{BF}, \quad (1)$$

where E_H is the reference energy of the pristine host cell. $E_D(q)$ is the energy of the supercell including the defect, D, with charge state q. E_i and μ_i are the reference energy and the chemical potential of element i, respectively, and n_i is the number of element i removed from the system. E_F is the Fermi level for which to evaluate the defect formation energies, while E_{VBM} refers this energy to the energy of the valence band maximum in the DFT calculations. Due to the limited supercell, three correction schemes, E_{corr}^{pot}, E_{corr}^{IC}, and E_{corr}^{BF}, are employed to correct for finite size effects. The potential alignment correction, E_{corr}^{pot}, aligns the potential of the defect cell to that of the defect free host cell [58], and the image charge correction, E_{corr}^{IC}, corrects for the interactions between the defect and the charge of its periodic image [58,59]. Lastly, the band filling correction, E_{corr}^{BF}, corrects for the unphysical filling of holes and electrons in the valence and conduction band, respectively [58,60].

The thermodynamic stability regions of $CsGeCl_3$ and $CsGeI_3$, shown in SM [55] Figs. S6 and S7, are calculated by evaluating formation energies of all competing phases using the Chemical Potential Limits Analysis Program (`CPLAP`) [61]. To show the full defect chemistry of $CsGeCl_3$ and $CsGeI_3$, defect formation energies, shown in Figs. 4(a) and 4(b), are calculated using three sets of chemical potentials for both materials, indicated in SM [55] Figs. S6 and S7.

The mobility of V_{Cs} and V_X were investigated using the climbing image nudged elastic bands method [62,63] (ci-NEB) with five images between the initial and final image. For comparison, the migration barriers were calculated in supercells with charged and neutral defects. Two different migration paths for V_X, displayed in SM [55] Fig. S9, were investigated.

Lattice parameters for 71°, 109° and 180° DW cells for $CsGeX_3$ were calculated from the equations displayed in SM [55] Table S15 using the PBEsol optimized lattice parameters. To minimize DW-DW interactions, a-parameters of ∼75 Å were used. Γ-centred k-point meshes of $1 \times 4 \times 6$, $1 \times 4 \times 4$, $1 \times 6 \times 4$, and $1 \times 6 \times 4$ were used for the for 71°, 109°, and 180° Y- and X-type DW supercells, respectively. The atomic positions were relaxed until all forces on all ions were less than 0.001 eV Å^{-1}. DW supercells, for $CsGeCl_3$, with DFT optimized atomic positions are shown in SM [55] Fig. S11.

Investigations of defect segregation enthalpies were investigated by calculating the defect formation energies as a function of distance from a 71° DW in $CsGeCl_3$. To avoid defect-defect interactions the cross section area of the DW supercells was increased by a $1 \times 2 \times 3$ expansion and a Γ-centred k-point mesh of $1 \times 2 \times 2$ was used.

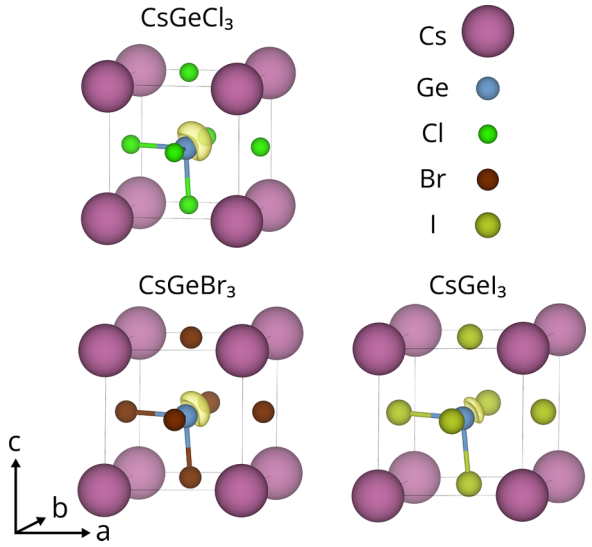


FIG. 1. DFT optimized primitive structures of $CsGeCl_3$, $CsGeBr_3$ and $CsGeI_3$ visualized together with their respective lone pairs. The lone pairs are extracted from the partial charge density of the top valence bands and shown with an isosurface level of 0.02. The polarization is in the [1,1,1] direction.

The mobility of DWs was investigated using the ci-NEB method with 5 images. A strict force criterion of 0.001 eV $Å^{-1}$ was used for optimising the atomic positions of the start and end images due to the flat energy landscape around the DW equilibrium position. ci-NEB calculations were performed with a force criterion of 0.01 eV $Å^{-1}$. Point defect pinning was studied for 71° DWs in $CsGeCl_3$ by calculating migration barriers across point defects in DW supercells. The supercells used are described in SM [55] Table S16 and Fig. S17 and a Γ-centred k-point mesh of $1 \times 2 \times 2$ and a force criterion of 0.01 eV $Å^{-1}$ was used for structure optimization.

III. RESULTS

The structural properties of the relaxed primitive cells, see Fig. 1, were calculated and are presented in Table I. Our calculated lattice parameters show good agreement with experimental values reported in the literature [11,19,64,65]. The HSE06 functional gives values closest to experiments, with only a subtle overestimation. In contrast, PBEsol slightly underestimates the lattice parameters, but achieves excellent agreement with experimental data when thermal expansion and related effects are considered. Estimated polarization using formal charges (FC), Born effective charges (BEC) and Berry phase calculations are shown in Table II and show a decreasing polarization from $CsGeCl_3$ to $CsGeI_3$. The Berry phase method suggests significantly larger polarizations than using BEC and the point charge model, indicating significant contribution from electrons and the Ge lone pair. Our values are relatively close to what has been reported previously using the PBE functional [10].

A. Electronic structure

Partial and total electronic density of states (DOS) are calculated for $CsGeX_3$ and displayed in Fig. 2. The

TABLE II. Tolerance factor, polarization, band gaps, and effective masses of holes and electrons calculated for $CsGeX_3$ (X = Cl, Br, I) using the HSE06 functional. Born effective charges are calculated using the finite differences method.

	$CsGeCl_3$	$CsGeBr_3$	$CsGeI_3$
t	1.027	1.009	0.985
P_{FC} (μC/cm^2)	8.5	7.6	6.9
P_{BEC} (μC/cm^2)	10.84	10.47	9.88
P_{Berry} (μC/cm^2)	24.3	21.3	21.0
E_g (eV)	3.015	2.068	1.438
m_h^*	0.325	0.189	0.138
m_e^*	0.438	0.187	0.134

conduction band minimum (CBM) consist mainly of Ge p states with some covalency with X p. The valence band maximum (VBM) show mixing of Ge s, Ge p, and X p. The Ge lone pair can be seen at the top of the valence band as hybridization between Ge s and Ge p. The lone pair causes an off-centering of the Ge ions and, thus, noncentrosymmetry and ferroelectricity in these halide perovskites.

The strength (stereochemical activity) of the lone pair can be determined by the overlap between Ge s and X p as good overlap results in mainly nonbonding Ge s states that are high enough in energy for hybridization with Ge p. The overlap between Ge s and X p and the lone pair are shown in detail in SM [55] Fig. S4. The degree of covalency between Ge s and X p has been quantified by calculating the X p contribution to the covalency between Ge s and X p at around −9 eV in

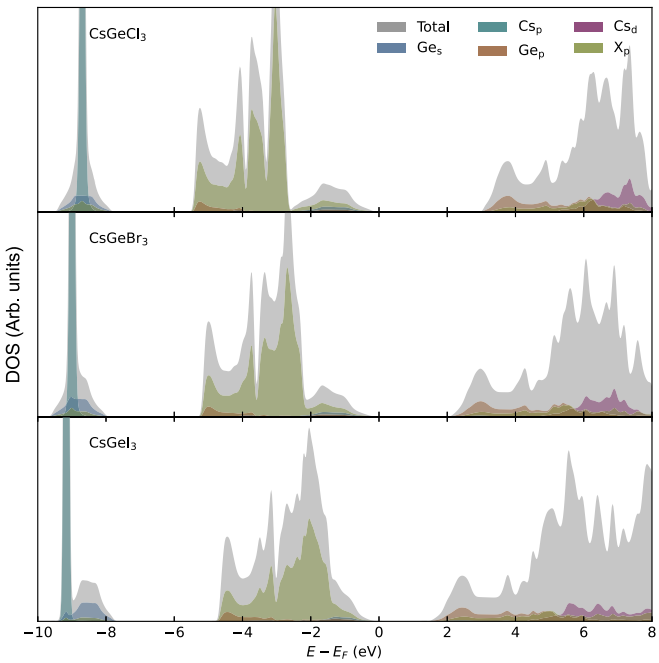


FIG. 2. Electronic density of states for $CsGeCl_3$, $CsGeBr_3$, and $CsGeI_3$ calculated using the HSE06 functional. Cs p, Cs d, Ge s, Ge p, and X p (halogen-p) are shown and colored in turquoise, purple, blue, orange and green, respectively. Other orbitals do not contribute significantly and are, thus, omitted.

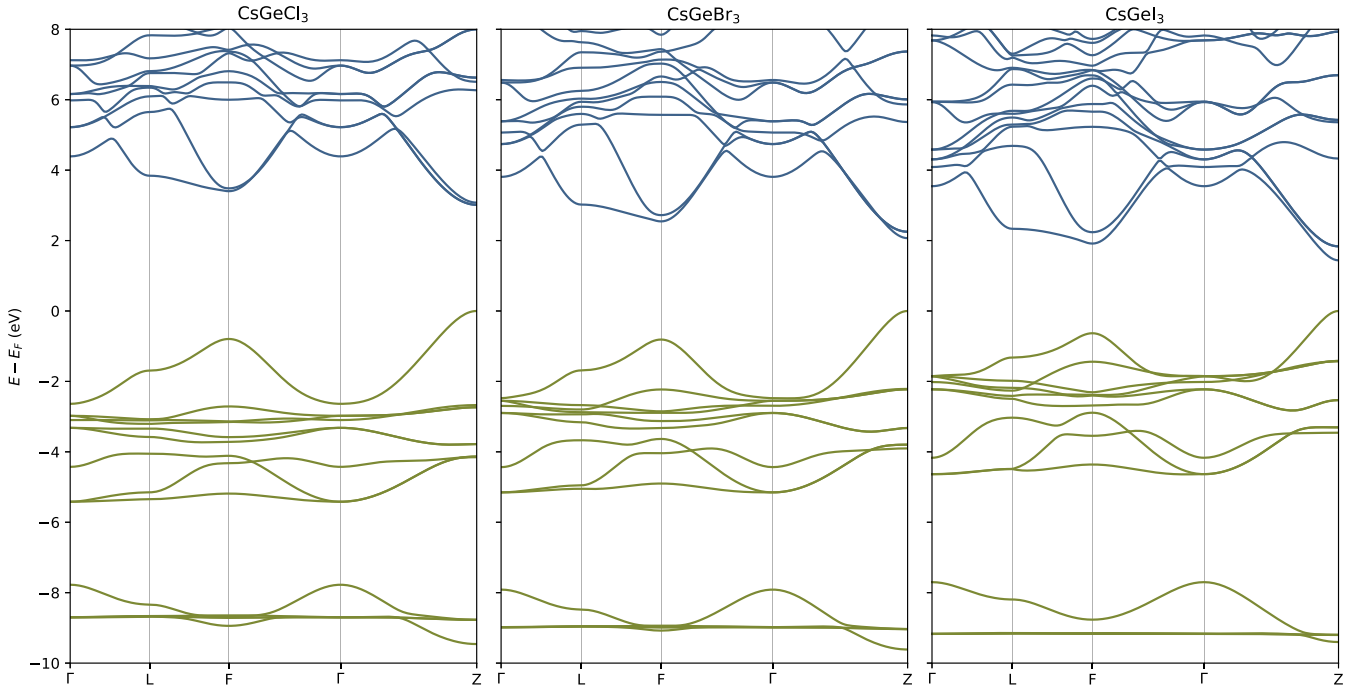


FIG. 3. Electronic band structures for $CsGeCl_3$, $CsGeBr_3$, and $CsGeI_3$ calculated using the HSE06 functional. The valence and conduction band are colored in green and blue, respectively.

a similar fashion as what was done by Payne *et al.* for a series of post-transition metal oxides [66,67]. Calculated X *p* contribution of 0.34, 0.25, and 0.17 for $CsGeCl_3$, $CsGeBr_3$, and $CsGeI_3$, respectively, predicts stronger mixing and, thus, stronger lone pairs going from $CsGeI_3$ to $CsGeCl_3$. The energy of X *p* increases down the periodic table leading to less mixing of Ge *s* and X *p*, therefore weaker hybridization between Ge *s* and Ge *p*, and a weaker lone pair. The evaluated lone pair strength correlates nicely with decreasing band gaps and polarization from $CsGeCl_3$ to $CsGeI_3$. DOS-es calculated using the PBEsol functional show very similar trends and are displayed in SM [55] Fig. S2. To further illustrate the nature of the lone pairs, Fig. 1 shows the real-space projections of the charge density at the top of the valence band.

Calculated band structures, displayed in Fig. 3, show direct band gaps at Z of ∼3.0, 2.1, and 1.4 eV, slightly lower than experimental values reported for $CsGeCl_3$ and $CsGeBr_3$ [45]. From $CsGeCl_3$ to $CsGeI_3$, both the lattice parameters and Ge-X bond lengths increase, which is inversely correlated with the observed reduction in band gap. Moreover, calculated band structures show a large degree of curvature at the band edges and display large band gaps of around 4 eV at the Γ point demonstrating the importance of the *k*-point sampling [68]. Calculated effective masses, displayed in Table II, show exceptionally low values. According to the classification by Davies *et al.* [69], which characterizes the degree of polaronic behavior, $CsGeCl_3$ lies on the border between types I and II, while $CsGeBr_3$ and $CsGeI_3$ fall firmly within type I. Therefore, very high electron and hole mobilities are expected for $CsGeBr_3$ and $CsGeI_3$, whereas some degree of polaronic behavior is expected in $CsGeCl_3$. The PBEsol functional gives relatively similar band structures, see SM [55] Fig. S3, albeit significantly lower band gaps. The bottom two bands of the CB are almost degenerate at the F and Z points in $CsGeCl_3$, but less so in $CsGeBr_3$ and $CsGeI_3$. The localized bands at around −9 eV are Cs *p*, as seen in the DOS in Fig. 2.

B. Intrinsic defect thermodynamics

Defect formation energies as a function of the Fermi energy for $CsGeCl_3$ and $CsGeI_3$, calculated using the HSE06 functional, are displayed in Figs. 4(a) and 4(b). Each figure includes three panels showing the formation energies at three different parts of the stability window, indicated in SM [55] Figs. S6 and S7. Hybrid defect calculations were not performed for $CsGeBr_3$, as this compound is expected to exhibit intermediate properties between $CsGeCl_3$ and $CsGeI_3$.

Throughout the stability region, the defects with the lowest formation energies are V_{Cs}, V_{Ge}, and V_X. Halide interstitials show relatively high formation energies, and therefore, V_X are expected to be the dominant halide defects. Cation antisites, with the exception of Ge_{Cs} in panel (b), show high formation energies, due to the difference in charge and size (0.73 Å, 1.88 Å [70]) between Cs and Ge ions.

All *n*-type defects show deep transition levels while several *p*-type defects display shallow or resonant defect levels. V_{Cs} show shallow defect levels (−1/0) of 0.004 and 0.015 eV above the VBM in $CsGeCl_3$ and $CsGeI_3$, respectively, while V_{Ge} is deep in $CsGeCl_3$ and resonant in $CsGeI_3$. At the halogen rich limit (left panels), the Fermi level is pinned at approximately 0.4 and 0.07 eV above the VBM for $CsGeCl_3$ and $CsGeI_3$, respectively. Both materials show *p*-type dopability at this part of the stability region. Towards the halogen poor edge, the Fermi level shifts towards

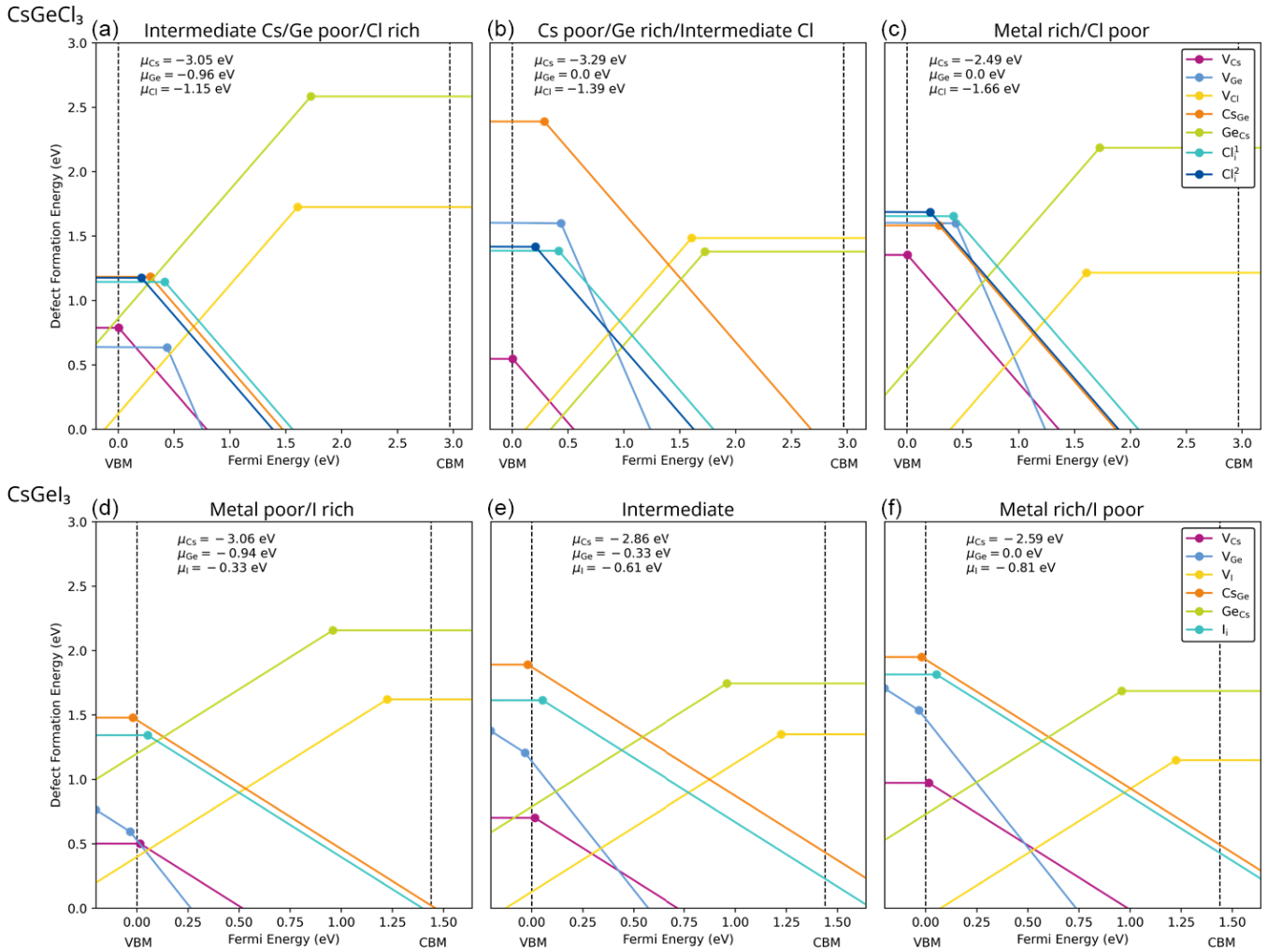


FIG. 4. Thermodynamic transition level diagrams for intrinsic defects in bulk $CsGeCl_3$ (a) and $CsGeI_3$ (b) calculated using the HSE06 functional. The three panels for each compound show the transition levels at three different chemical environments indicated in the stability window shown in SM [55] Figs. S6 and S7. The dashed lines at 0 eV, and ∼3 and ∼1.5 eV display the VBM and CBM, respectively.

the middle of the band gap and less *p*-type character is observed.

Point defects and *p*-type conductivity in $CsGeCl_3$ have previously been investigated, using DFT with the PBE functional, by Huang *et al.* [27]. Despite the different functional, our calculations show similar results to what they report, but as expected, the HSE06 functional gives deeper transition levels as HSE06 is known to better localize holes and electrons. Using the HSE06 functional also results in subtly larger formation energies on average.

Calculated migration barriers for V_{Cs} and V_{Cl} in both neutral and charged supercells of $CsGeCl_3$ are displayed in Fig. 5. V_{Cs} show relatively low migration barriers of ∼0.75 eV, while V_{Cl} display very low migration barriers comparable with V_{Li} and V_{Na} in the best solid state batteries [71,72]. For the charged defects, the migration barriers are ∼0.22 eV and ∼0.24 eV, and neutral defects, ∼0.30 eV and ∼0.33 eV for paths I and II, respectively. Path I is between two Cl sites with their short Ge-Cl bonds to the same Ge atom while path II is between two Cl sites with their short bonds to two different Ge atoms. Both paths are displayed in SM [55] Fig. S9. Migration of neutral V_{Cl} through path II shows an additional small barrier due to polaron hopping.

V_{Cs} and V_I in $CsGeI_3$ show very similar migration barriers to what is shown for $CsGeCl_3$, see SM [55] Fig. S8. Mobile ions are known as one of the main contributors to the degradation of halide perovskite solar cells [73,74], with reported migration barrier for V_I in methylammonium lead iodide ($CH_3NH_3PbI_3$) ranging broadly from 0.08 eV [75] to 0.6 eV [76].

C. Domain walls

Calculated DW energies, summarized in Table III, indicate that 71° DWs are the most favorable type in $CsGeX_3$, closely followed by 109° DWs. Both exhibit minimal structural distortion and form narrow walls, as visualized for $CsGeCl_3$ in Fig. 6, with additional structural parameters displayed in SM [55] Figs. S12, S13, and S14 for $CsGeCl_3$, $CsGeBr_3$, and $CsGeI_3$, respectively. In contrast, 180° DWs induce significant lattice distortions, resulting in substantially higher DW energies. Notably, the energies of 71° and 109° DWs in $CsGeX_3$

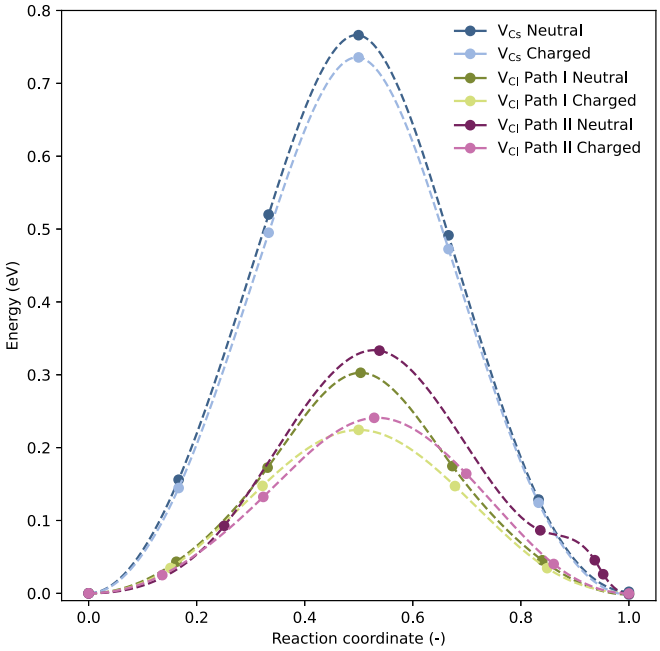


FIG. 5. Migration barriers of V_{Cs} and V_{Cl} in bulk $CsGeCl_3$ in charged and neutral cells calculated using the PBEsol functional.

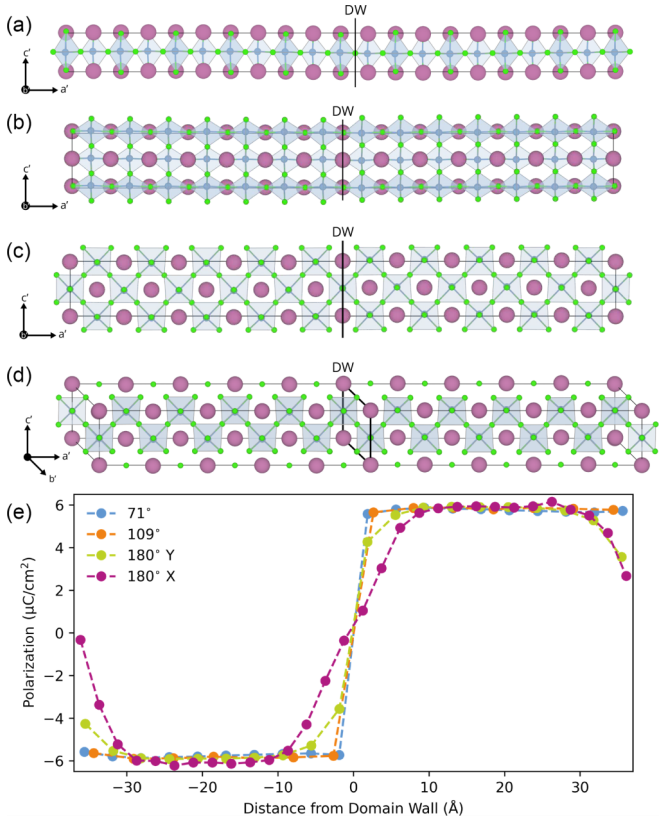


FIG. 6. PBEsol optimized 71° (a), 109° (b), 180° Y-type (c), and 180° X-type (d) ferroelectric domain walls in $CsGeCl_3$. Estimated polarizations, from formal charges using the point charge model, are displayed in (e) as a function of the supercell dimension perpendicular to the domain walls. The relation between the supercells' and primitive cells lattice parameters is shown in SM [55] Table S15.

are considerably lower than those reported for most ferroelectric oxide perovskites. For comparison, reported DW energies for 180° DWs in $LiNbO_3$, 109° DWs in $BiFeO_3$, 90° DWs in PbTiO3, 90° DWs in orthorhombic $KNbO_3$, and 71° and 109° DWs in $BaTiO_3$ are 141 [77], 33 [78], 35 [79], 4.3 [80], 3.8 [81], and 11.1 [81] mJ/m^2, respectively. DW energies reported for the metal-organic halide perovskite $MAPbX_3$ (X = Cl, Br, I) are 3, 1, and 8 mJ/m^2 [82], respectively, which are comparable to those found in this study.

As there are only subtle distortions associated with the low-energy DWs, there are almost no changes to the interatomic distances and bonding, and therefore almost no changes in the electronic structure are observed at the DWs, see SM [55] Fig. S15. Therefore, no reduction in bandgap at the DWs in $CsGeX_3$ is expected and also not observed.

D. Interactions between point defects and domain walls

The 71° DWs in $CsGeCl_3$ were selected as the model system for investigating interactions between point defects and DWs, in order to reduce both complexity and computational cost. Given the similar behavior of point defects (Figs. 4 and 5, as well as in SM [55] Fig. S8) and DWs (Table III, SM [55]

TABLE III. Calculated domain wall energies for DWs in $CsGeCl_3$, $CsGeBr_3$, and $CsGeI_3$ calculated using the PBEsol functional.

DW-type	$CsGeCl_3$ (mJ/m^2)	$CsGeBr_3$ (mJ/m^2)	$CsGeI_3$ (mJ/m^2)
71°	1.6	1.1	1.5
109°	1.7	4.2	2.5
180° Y	47	18	19
180° X	57	22	21

Figs. S12, S13, and S14) across these compounds, the interactions between point defects and DWs are also expected to be comparable. Moreover, as $CsGeCl_3$ exhibits larger structural distortions, higher polarization, stronger lone pair activity, and more pronounced polaronic behavior, the interactions between point defects and DWs in $CsGeCl_3$ is expected to be more significant than in the other compounds. The 71° DW was chosen because it has the lowest formation energy for the compounds considered, making it the most likely to form.

SM [55] Fig. S16 shows binding energies between point defects and a 71° DW in $CsGeCl_3$. None of the investigated point defects show any significant binding energies. V_{Ge} show the largest binding energy, but only on the order of ~0.005 eV, which is below the thermal energy (k_BT) at room temperature. Both V_{Cs} and V_{Ge} show a decrease in the binding energy approaching the DW before it increases at the DW. However, these changes are very small and not likely to have any experimental significance.

Point defects typically exhibit reduced defect formation energies at DWs, due to the inherent strain fields and distortions associated with the DWs [37,77,83,84]. Generally, point defects accumulate at DWs to maximize the volume of unperturbed bulk material, under the condition that the local structural distortions caused by DWs and the point defects are compatible [83,85]. However, as the distortions accompanying

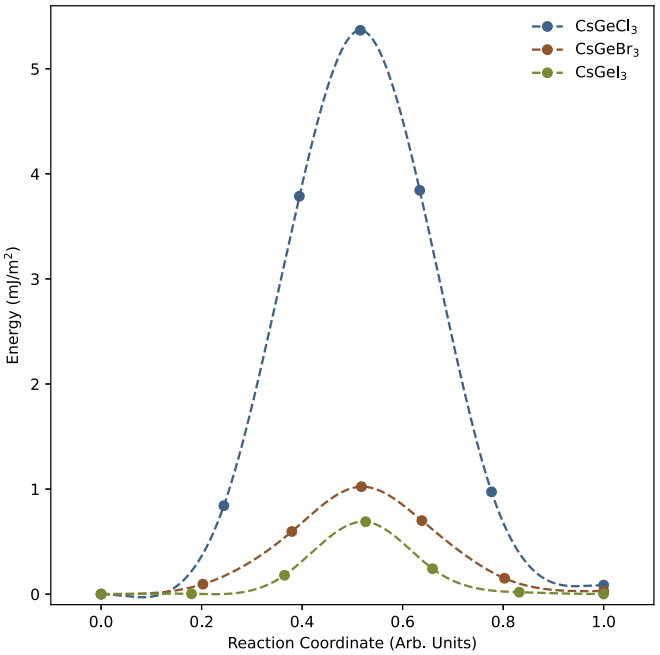


FIG. 7. Calculated migration barriers for 71° DWs in $CsGeCl_3$, $CsGeBr_3$, and $CsGeI_3$ using the PBEsol functional and the ci-NEB method.

the low-energy DWs in $CsGeX_3$ are very subtle, almost no change in defect formation energies is observed at the 71° DWs in $CsGeCl_3$.

Migration barriers for 71° DWs in $CsGeCl_3$, $CsGeBr_3$, and $CsGeI_3$ without point defects are displayed in Fig. 7. The figure shows very low migration barriers for 71° DWs, with migration barriers of ∼5.4, 1.0, and 0.7 mJ/m^2 for $CsGeCl_3$, $CsGeBr_3$, and $CsGeI_3$, respectively. These are all significantly lower than values reported for ferroelectric oxides, where, for example, 180° DWs in $h-YMnO_3$, $LiNbO_3$, and $PbTiO_3$ are reported with migration barriers of ∼30 [83,86], 35 [77], and 37 [79] mJ/m^2. $CsGeCl_3$ show a migration barrier larger than the energy required to form the DW. Calculating the migration barriers of 109° DWs was also attempted, but while "moving" each DW just transforms into two 71° DWs. The weak interaction between DWs and point defects is also reflected in the calculated DW migration barriers shown in Fig. 8. The figure shows calculated migration barriers for a 71° DW in $CsGeCl_3$ with and without point defects in the supercell. The position of the defects is indicated by the filled circles and the DWs are moved in two steps: first approaching the defect, then moving past it. The interactions between the DW and defects are investigated using neutral and charged cells. The point defects studied are V_{Cs}, V_{Ge}, and in-plane and out-of-plane V_{Cl}, as well as $V_{Cs} + V_{Cl}$ defect pairs.

V_{Cs} results in an increased migration barrier of almost 40%, however, the migration barriers are still very small. There is also a subtle increase in the migration barrier for the DW moving to the defect. Additionally, introducing a compensating hole into the system does not alter the results.

Also, for V_{Ge}, there is no significant difference between calculations performed with or without hole compensation. V_{Ge} does not result in any increase in migration barriers, but, as seen in the figure, the DW prefers to be situated where the defect is located. A small reduction in the total energy is also observed, similar to what is shown in SM [55] Fig. S16, when the DW coincides with the position of the V_{Ge}.

The two inequivalent V_{Cl} affect the DW very differently. An in-plane neutral V_{Cl} leads to a substantial increase of the migration barrier of about 400%. In contrast, when the in-plane V_{Cl} is not compensated by an electron, the DW prefers to be co-located with the defect. For the out-of-plane V_{Cl}, there is no change in the migration barrier for the charged defect, while neutral charge state results in a similar increase in the migration barrier as observed for V_{Cs}.

During the movement of a 71° domain wall, one in-plane Ge-Cl bond is formed while another bond is broken. If a neutral in-plane V_{Cl} is present at the domain wall, the polaron that compensates the defect must also transfer from one Ge atom to another, explaining the substantially increased migration barrier resulting from this specific point defect.

The investigated defect clusters show combined characteristics of the individual defects in the charged unit cells. V_{Cs} together with in-plane V_{Cl} show increased migration barriers, similar to V_{Cs}, and a preference for the in-plane V_{Cl}. V_{Cs}, together with out-of-plane V_{Cl}, show increased migration barriers relatively similar to just a combination of the increased migration barriers of the individual defects.

IV. DISCUSSION

The potential of $CsGeCl_3$ as a transparent *p*-type conductor has previously been discussed in work by Huang *et al.* [27], who highlighted its high hole mobility, as well as favorable formation energy and transition level of *p*-type V_{Ge}. Our hybrid functional calculations support their findings regarding the high hole mobility and low formation energy of V_{Ge}. However, using the HSE06 functional, we find that V_{Ge} exhibits a significantly deeper transition level than previously reported (∼0.5 eV) [27]. In contrast, V_{Cs} displays both a shallow transition level and low formation energy. For $CsGeI_3$, both V_{Cs} and V_{Ge} show low formation energies, shallow transition levels, and even lower hole effective masses. These results indicate that both materials are promising candidates for *p*-type conductivity. Additionally, at specific chemical environments the energy of *n*-type defects, namely V_X, is sufficiently high that the introduction of a good *p*-type dopant can pin the Fermi level within the valence band. Regarding transparent conductivity, $CsGeCl_3$ show a band gap close to the energy of visible light, and has been reported experimentally with an even larger band gap [87], as well as forming colorless crystals [11].

Calculated migration barriers for neutral V_{Cl} and 71° DWs over neutral V_{Cl} show larger migration barriers than migration barriers calculated with charged defects, see Figs. 5 and 8. This means that the extra electron in the cells containing neutral V_{Cl} affects both the mobility of halogen vacancies, as well as the DW mobility. This is likely due to the extra electron populating anti-bonding Ge *p* states, destabilising the lone pair. For a charged defect, the lone pair is able to rotate more freely about its parent Ge ion and we hypothesize that this helps stabilising V_{Cl} in the intermediate states, thus reducing the energy of the transition state.

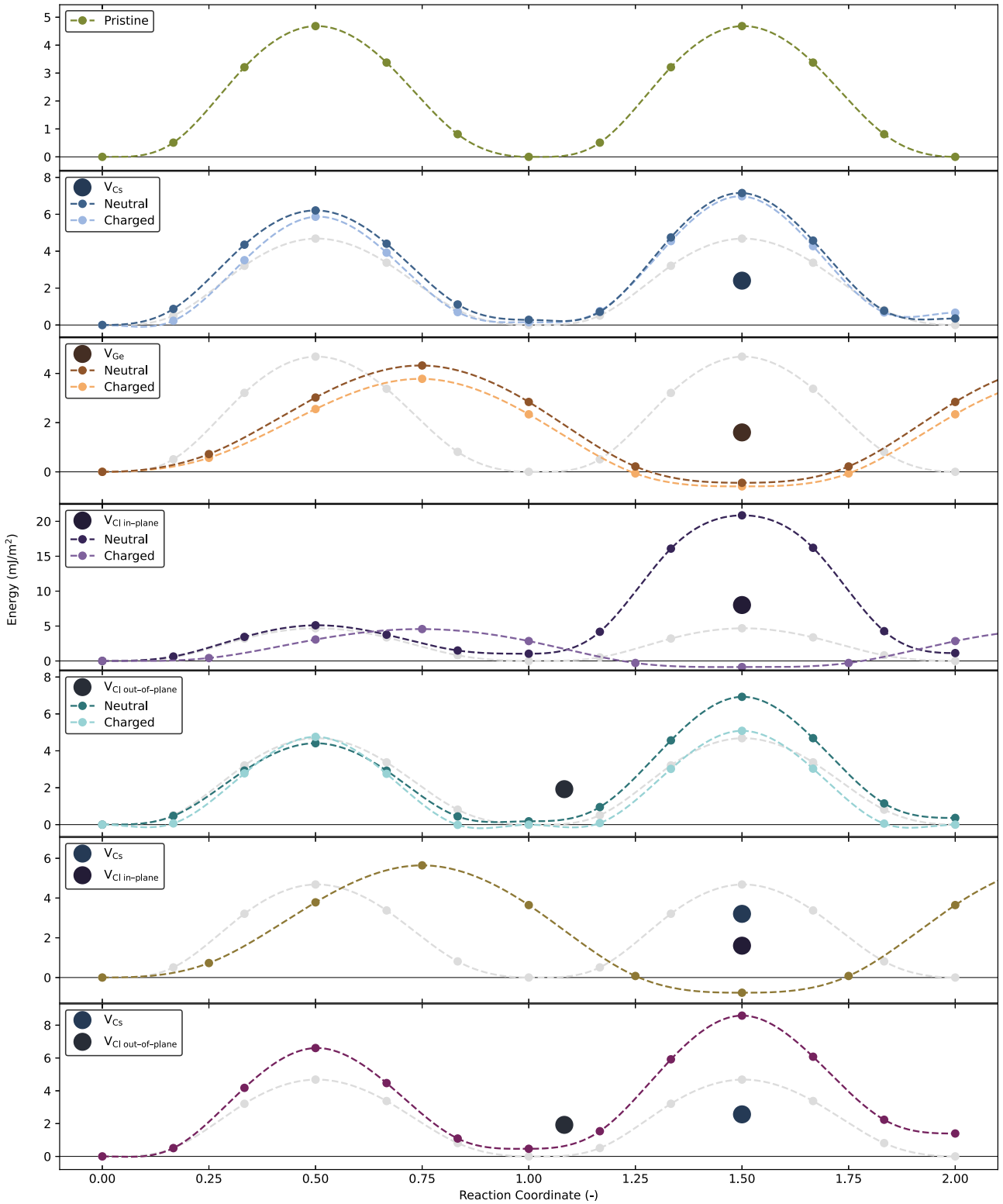


FIG. 8. DW migration barriers for 71° DWs in $CsGeCl_3$ with and without defects in its vicinity. The first plot shows the migration barrier in the pristine DW cell. The next four plots show migration barriers in cells with V_{Cs}, V_{Ge}, V_{Cl}, and V_{Cl}, respectively. The gray dashed curves indicate the migration barrier in the pristine cell. For V_{Cs}, V_{Ge}, V_{Cl}, migration barriers are estimated both in neutral and charged cells. The two bottom panels display DW migration barriers with a defect pair in the cell. The filled circles indicate the position of the point defects.

Furthermore, both V_{Cl} migration through path II and DW migration past an in-plane V_{Cl} in neutral cells, require electron transfer between two Ge atoms (see SM [55] Fig. S10). In $CsGeCl_3$, the deep transition level of V_{Cl} suggests an electron transfer through polaron hopping. The migration barrier associated with the polaron hopping will add to the total migration barrier, which explains the increased energy barriers of these migrations.

In contrast, in $CsGeI_3$, there is no difference in V_I migration barriers for the different paths (SM [55] Fig. S8). V_I shows a significantly more shallow defect level than V_{Cl} and using PBEsol, the compensating electron is predominantly delocalized and, thus, no increase in migration barrier for path II is observed. Ultimately, calculations with neutral n-type defects are likely not important as these materials show a strong *p*-type character and V_{Cl} will instead be compensated by other defects rather than electrons.

DWs in $CsGeX_3$ show low formation energies, as well as low migration barriers. However, because of the subtlety of the structural distortions across the DWs, no significant change in point defect formation energy or electronic structure is observed at the DW. It is therefore likely difficult to obtain exotic electronic properties at the DWs of these materials. Despite the low defect formation energies, shallow transition levels, low defect migration barriers, and good carrier mobilities, this means that $CsGeX_3$ are unlikely to be promising candidates for DW-based electronics.

Instead, low DW migration barriers indicate low energy loss and joule heating during polarization reversal, and are, thus, useful for applications where high switching frequencies are needed, e.g., for FeRAMs, GHz transducers, and electro-optics.

V. CONCLUSION

Using hybrid functional DFT we have found that ferroelectric inorganic halides $CsGeX_3$ show highly mobile electrons and holes. The point defects V_{Cs} and V_X show low formation energies and low and very low, respectively, migration energy barriers. This implies that point defects should be very important to the functional properties of these materials. Furthermore, low formation energy *p*-type defects show shallow defect levels and there is a potential for *p*-type doping of this ferroelectric material with an electronic band gap almost large enough to make it transparent to visible light.

We have shown that 71° DWs exhibit very low formation energies, closely followed by 109° DWs. This is a consequence of the very subtle structural distortions found at these DWs compared to bulk, in contrast to the pronounced distortions often observed in oxide ferroelectrics. The absence of significant strain fields means that point defects show little tendency to accumulate at the DWs, and the electronic structure closely resembles that of the bulk. Consequently, $CsGeX_3$ is unlikely to be suitable for DW-based electronics.

However, the low formation energy of the DWs, and especially the remarkably high mobility of 71° DWs, make $CsGeX_3$ materials promising candidates for applications as ferroelectrics that require high-frequency switching with low energy dissipation. The insensitivity to point defects and the inclination towards *p*-type doping emphasizes the different properties and technological potential of ferroelectric halide perovskites compared to oxide perovskites.

ACKNOWLEDGMENTS

Financial support for this project was provided from the Research Council of Norway through Projects No. 302506, No. 301954, and No. 354614. Computational resources were provided through Project No. NN9264K at Sigma2 - the National Infrastructure for High-Performance Computing and Data Storage in Norway.

DATA AVAILABILITY

Structure files for unit cells and supercells with domain walls are openly available [88].

[1] M. M. Lee, J. Teuscher, T. Miyasaka, T. N. Murakami, and H. J. Snaith, Efficient hybrid solar cells based on meso-superstructured organometal halide perovskites, Science **338**, 643 (2012).

[2] S. D. Stranks, G. E. Eperon, Giulia Grancini, C. Menelaou, M. J. P. Alcocer, T. Leijtens, L. M. Herz, A. Petrozza, and H. J. Snaith, Electron-hole diffusion lengths exceeding 1 micrometer in an organometal trihalide perovskite absorber, Science **342**, 341 (2013).

[3] L. Protesescu, S. Yakunin, M. I. Bodnarchuk, F. Krieg, R. Caputo, C. H. Hendon, R. X. Yang, A. Walsh, and M. V. Kovalenko, Nanocrystals of cesium lead halide perovskites ($CsPbX_3$, X = Cl, Br, and I): Novel optoelectronic materials showing bright emission with wide color gamut, Nano Lett. **15**, 3692 (2015).

[4] M. A. Green, A. Ho-Baillie, and H. J. Snaith, The emergence of perovskite solar cells, Nat. Photon. **8**, 506 (2014).

[5] J. M. Frost, K. T. Butler, and A. Walsh, Molecular ferroelectric contributions to anomalous hysteresis in hybrid perovskite solar cells, APL Mater. **2**, 081506 (2014).

[6] J. M. Frost, K. T. Butler, F. Brivio, C. H. Hendon, M. van Schilfgaarde, and A. Walsh, Atomistic origins of high-performance in hybrid halide perovskite solar cells, Nano Lett. **14**, 2584 (2014).

[7] H.-S. Kim, S. K. Kim, B. J. Kim, K.-S. Shin, M. K. Gupta, H. S. Jung, S.-W. Kim, and N.-G. Park, Ferroelectric polarization in $CH_3NH_3PbI_3$ perovskite, J. Phys. Chem. Lett. **6**, 1729 (2015).

[8] Y. Kutes, L. Ye, Y. Zhou, S. Pang, Bryan D. Huey, and N. P. Padture, Direct observation of ferroelectric domains in solution-processed $CH_3NH_3PbI_3$ perovskite thin films, J. Phys. Chem. Lett. **5**, 3335 (2014).

[9] B. Chen, M. Yang, S. Priya, and K. Zhu, Origin of J–V hysteresis in perovskite solar cells, J. Phys. Chem. Lett. **7**, 905 (2016).

[10] Y. Zhang, E. Parsonnet, A. Fernandez, S. M. Griffin, H. Huyan, C.-K. Lin, T. Lei, J. Jin, E. S. Barnard, A. Raja, P. Behera, X. Pan, R. Ramesh, and P. Yang, Ferroelectricity in a semiconducting all-inorganic halide perovskite, Sci. Adv. **8**, eabj5881 (2022).

[11] A. N. Christensen and S. E. Rasmussen, A ferroelectric chloride of perowskite type. Crystal structure of $CsGeCl_3$, Acta Chem. Scand. **19**, 421 (1965).

[12] P. Marton, I. Rychetsky, and J. Hlinka, Domain walls of ferroelectric $BaTiO_3$ within the Ginzburg-Landau-Devonshire phenomenological model, Phys. Rev. B **81**, 144125 (2010).

[13] R. E. Cohen, Origin of ferroelectricity in perovskite oxides, Nature (London) **358**, 136 (1992).

[14] W. J. Merz, The electric and optical behavior of $BaTiO_3$ single-domain crystals, Phys. Rev. **76**, 1221 (1949).

[15] M. Budimir, D. Damjanovic, and N. Setter, Piezoelectric anisotropy-phase transition relations in perovskite single crystals, J. Appl. Phys. **94**, 6753 (2003).

[16] G. Shirane, H. Danner, A. Pavlovic, and R. Pepinsky, Phase transitions in ferroelectric $KNbO_3$, Phys. Rev. **93**, 672 (1954).

[17] M. D. Maeder, D. Damjanovic, and N. Setter, Lead free piezoelectric materials, J. Electroceram. **13**, 385 (2004).

[18] K. P. Ong, T. W. Goh, Q. Xu, and A. Huan, Structural evolution in methylammonium lead iodide $CH_3NH_3PbI_3$, J. Phys. Chem. A **119**, 11033 (2015).

[19] G. Thiele, H. W. Rotter, and K. D. Schmidt, Kristallstrukturen und Phasentransformationen von Caesiumtrihalogenogermanaten(II) $CsGeX_3$ (X = Cl, Br, I), Z. anorg. allg. Chem. **545**, 148 (1987).

[20] L.-C. Tang, C.-S. Chang, L.-C. Tang, and J. Y. Huang, Electronic structure and optical properties of rhombohedral $CsGeI_3$ crystal, J. Phys.: Condens. Matter **12**, 9129 (2000).

[21] D. Ray, C. Clark, H. Q. Pham, J. Borycz, R. J. Holmes, E. S. Aydil, and L. Gagliardi, Computational study of structural, electronic properties of lead-free $CsMI_3$ perovskites (M = Ge, Sn, Pb, Mg, Ca, Sr, and Ba), J. Phys. Chem. C **122**, 7838 (2018).

[22] S. Bouhmaidi, A. Marjaoui, A. Talbi, M. Zanouni, K. Nouneh, and L. Setti, A DFT study of electronic, optical, and thermoelectric properties of Ge-halide perovskites $CsGeX_3$ (X = F, Cl, and Br), Comput. Condens. Matter **31**, e00663 (2022).

[23] A. Popoola, N. Maity, R. Kashikar, S. Lisenkov, and I. Ponomareva, Large electrically and chemically tunable Rashba-Dresselhaus effects in ferroelectric $CsGeX_3$ (X = Cl, Br, I) perovskites, J. Phys. Chem. C **128**, 17806 (2024).

[24] B. T. Ayalew, S. G. Kuma, and B. B. Haile, Structural, electronic, and transport properties of $CsGeX_3$ (X = Cl, Br, I) for energy storage and hybrid solar cell applications, Comput. Condens. Matter **43**, e01043 (2025).

[25] M. E. Akkel and H. Ez-Zahraouy, Tuning the photocatalytic performance of halide perovskites for efficient solar hydrogen production: A DFT study of $CsGeCl_{3-x}X_x$ (X = Br, I), Solid State Commun., **394**, 115721 (2024).

[26] N. F. Quackenbush, J. P. Allen, D. O. Scanlon, S. Sallis, J. A. Hewlett, A. S. Nandur, B. Chen, K. E. Smith, C. Weiland, D. A. Fischer, J. C. Woicik, B. E. White, G. W. Watson, and L. F. J. Piper, Origin of the bipolar doping behavior of SnO from x-ray spectroscopy and density functional theory, Chem. Mater. **25**, 3114 (2013).

[27] D. Huang, Y.-J. Zhao, Z.-P. Ju, L.-Y. Gan, X.-M. Chen, C.-S. Li, C. m. Yao, and J. Guo, First-principles prediction of a promising p-type transparent conductive material $CsGeCl_3$, Appl. Phys. Express **7**, 041201 (2014).

[28] M. W. Swift and J. L. Lyons, Lone-pair stereochemistry induces ferroelectric distortion and the Rashba effect in inorganic halide perovskites, Chem. Mater. **35**, 9370 (2023).

[29] J. Seidel, L. W. Martin, Q. He, Q. Zhan, Y.-H. Chu, A. Rother, M. E. Hawkridge, P. Maksymovych, P. Yu, M. Gajek, N. Balke, S. V. Kalinin, S. Gemming, F. Wang, G. Catalan, J. F. Scott, N. A. Spaldin, J. Orenstein, and R. Ramesh, Conduction at domain walls in oxide multiferroics, Nat. Mater. **8**, 229 (2009).

[30] D. Meier and S. M. Selbach, Ferroelectric domain walls for nanotechnology, Nat. Rev. Mater. **7**, 157 (2022).

[31] G. F. Nataf, M. Guennou, J. M. Gregg, D. Meier, J. Hlinka, E. K. H. Salje, and J. Kreisel, Domain-wall engineering and topological defects in ferroelectric and ferroelastic materials, Nat. Rev. Phys. **2**, 634 (2020).

[32] M. Schröder, A. Haußmann, A. Thiessen, E. Soergel, T. Woike, and L. M. Eng, Conducting domain walls in lithium niobate single crystals, Adv. Funct. Mater. **22**, 3936 (2012).

[33] J. Schultheiß, J. Schaab, D. R. Småbråten, S. H. Skjærvø, E. Bourret, Z. Yan, S. M. Selbach, and D. Meier, Intrinsic and extrinsic conduction contributions at nominally neutral domain walls in hexagonal manganites, Appl. Phys. Lett. **116**, 262903 (2020).

[34] D. R. Småbråten, Q. N. Meier, S. H. Skjærvø, K. Inzani, D. Meier, and S. M. Selbach, Charged domain walls in improper ferroelectric hexagonal manganites and gallates, Phys. Rev. Mater. **2**, 114405 (2018).

[35] D. Meier, J. Seidel, A. Cano, K. Delaney, Y. Kumagai, M. Mostovoy, N. A. Spaldin, R. Ramesh, and M. Fiebig, Anisotropic conductance at improper ferroelectric domain walls, Nat. Mater. **11**, 284 (2012).

[36] T. Rojac, A. Bencan, G. Drazic, N. Sakamoto, H. Ursic, B. Jancar, G. Tavcar, M. Makarovic, J. Walker, B. Malic, and D. Damjanovic, Domain-wall conduction in ferroelectric $BiFeO_3$ controlled by accumulation of charged defects, Nat. Mater. **16**, 322 (2017).

[37] J. Schaab, S. H. Skjærvø, S. Krohns, X. Dai, M. E. Holtz, A. Cano, M. Lilienblum, Z. Yan, E. Bourret, D. A. Muller, M. Fiebig, S. M. Selbach, and D. Meier, Electrical half-wave rectification at ferroelectric domain walls, Nat. Nanotechnol. **13**, 1028 (2018).

[38] J. Guyonnet, I. Gaponenko, S. Gariglio, and P. Paruch, Conduction at domain walls in insulating $Pb(Zr_{0.2}Ti_{0.8})O_3$ thin films, Adv. Mater. **23**, 5377 (2011).

[39] C. C. Stoumpos, C. D. Malliakas, and M. G. Kanatzidis, Semiconducting tin and lead iodide perovskites with organic cations: Phase transitions, high mobilities, and near-infrared photoluminescent properties, Inorg. Chem. **52**, 9019 (2013).

[40] J. Kang and L.-W. Wang, High defect tolerance in lead halide perovskite $CsPbBr_3$, J. Phys. Chem. Lett. **8**, 489 (2017).

[41] M. V. Kovalenko, L. Protesescu, and M. I. Bodnarchuk, Properties and potential optoelectronic applications of lead halide perovskite nanocrystals, Science **358**, 745 (2017).

[42] D. Cahen, L. Kronik, and G. Hodes, Are defects in lead-halide perovskites healed, tolerated, or both? ACS Energy Lett. **6**, 4108 (2021).

[43] A. M. Ganose, D. O. Scanlon, A. Walsh, and R. L. Z. Hoye, The defect challenge of wide-bandgap semiconductors for photovoltaics and beyond, Nat. Commun. **13**, 4715 (2022).

[44] J. Ye, N. Mondal, B. P. Carwithen, Y. Zhang, L. Dai, X.-B. Fan, J. Mao, Z. Cui, P. Ghosh, C. Otero-Martínez, L. v. Turnhout, Y.-T. Huang, Z. Yu, Z. Chen, N. C. Greenham, S. D. Stranks, L. Polavarapu, A. Bakulin, A. Rao, and R. L. Z. Hoye, Extending the defect tolerance of halide perovskite nanocrystals to hot carrier cooling dynamics, Nat. Commun. **15**, 8120 (2024).

[45] U. Schwarz, F. Wagner, K. Syassen, and H. Hillebrecht, Effect of pressure on the optical-absorption edges of $CsGeBr_3$ and $CsGeCl_3$, Phys. Rev. B **53**, 12545 (1996).

[46] G. Kresse and J. Hafner, *Ab initio* molecular dynamics for liquid metals, Phys. Rev. B **47**, 558 (1993).

[47] G. Kresse and J. Furthmüller, Efficiency of *ab initio* total energy calculations for metals and semiconductors using a plane-wave basis set, Comput. Mater. Sci. **6**, 15 (1996).

[48] G. Kresse and J. Furthmüller, Efficient iterative schemes for *ab initio* total-energy calculations using a plane-wave basis set, Phys. Rev. B **54**, 11169 (1996).

[49] P. E. Blöchl, Projector augmented-wave method, Phys. Rev. B **50**, 17953 (1994).

[50] G. Kresse and D. Joubert, From ultrasoft pseudopotentials to the projector augmented-wave method, Phys. Rev. B **59**, 1758 (1999).

[51] A. V. Krukau, O. A. Vydrov, A. F. Izmaylov, and G. E. Scuseria, Influence of the exchange screening parameter on the performance of screened hybrid functionals, J. Chem. Phys. **125**, 224106 (2006).

[52] A. J. Garza and G. E. Scuseria, Predicting band gaps with hybrid density functionals, J. Phys. Chem. Lett. **7**, 4165 (2016).

[53] B. G. Janesko, T. M. Henderson, and G. E. Scuseria, Screened hybrid density functionals for solid-state chemistry and physics, Phys. Chem. Chem. Phys. **11**, 443 (2009).

[54] J. P. Perdew, A. Ruzsinszky, G. I. Csonka, O. A. Vydrov, G. E. Scuseria, L. A. Constantin, X. Zhou, and K. Burke, Restoring the density-gradient expansion for exchange in solids and surfaces, Phys. Rev. Lett. **100**, 136406 (2008).

[55] See Supplemental Material at http://link.aps.org/supplemental/10.1103/bf5v-24b2 for Figs. S1–S17 and Tables S1–S16, which includes Refs. [61,66].

[56] A. M. Ganose, A. J. Jackson, and D. O. Scanlon, SUMO: Command-line tools for plotting and analysis of periodic *ab initio* calculations, J. Open Source Softw. **3**, 717 (2018).

[57] C. Freysoldt, B. Grabowski, T. Hickel, J. Neugebauer, G. Kresse, A. Janotti, and C. G. Van de Walle, First-principles calculations for point defects in solids, Rev. Mod. Phys. **86**, 253 (2014).

[58] S. Lany and A. Zunger, Assessment of correction methods for the band-gap problem and for finite-size effects in supercell defect calculations: Case studies for ZnO and GaAs, Phys. Rev. B **78**, 235104 (2008).

[59] S. T. Murphy and N. D. M. Hine, Anisotropic charge screening and supercell size convergence of defect formation energies, Phys. Rev. B **87**, 094111 (2013).

[60] C. G. Van de Walle and J. Neugebauer, First-principles calculations for defects and impurities: Applications to III-nitrides, J. Appl. Phys. **95**, 3851 (2004).

[61] J. Buckeridge, D. O. Scanlon, A. Walsh, and C. R. A. Catlow, Automated procedure to determine the thermodynamic stability of a material and the range of chemical potentials necessary for its formation relative to competing phases and compounds, Comput. Phys. Commun. **185**, 330 (2014).

[62] G. Henkelman, B. P. Uberuaga, and H. Jónsson, A climbing image nudged elastic band method for finding saddle points and minimum energy paths, J. Chem. Phys. **113**, 9901 (2000).

[63] G. Henkelman and H. Jónsson, Improved tangent estimate in the nudged elastic band method for finding minimum energy paths and saddle points, J. Chem. Phys. **113**, 9978 (2000).

[64] U. Schwarz, H. Hillebrecht, M. Kaupp, K. Syassen, H.-G. von Schnering, and G. Thiele, Pressure-induced phase transition in $CsGeBr_3$ studied by x-ray diffraction and Raman spectroscopy, J. Solid State Chem. **118**, 20 (1995).

[65] Z.-G. Lin, L.-C. Tang, and C.-P. Chou, Study on mid-IR NLO crystals $CsGe(Br_xCl_{1-x})_3$, Opt. Mater. (Amsterdam) **31**, 28 (2008).

[66] D. J. Payne, R. G. Egdell, A. Walsh, G. W. Watson, J. Guo, P.-A. Glans, T. Learmonth, and K. E. Smith, Electronic origins of structural distortions in post-transition metal oxides: Experimental and theoretical evidence for a revision of the lone pair model, Phys. Rev. Lett. **96**, 157403 (2006).

[67] A. Walsh, D. J. Payne, R. G. Egdell, and G. W. Watson, Stereochemistry of post-transition metal oxides: Revision of the classical lone pair model, Chem. Soc. Rev. **40**, 4455 (2011).

[68] N. Thi Han, V. K. Dien, and M.-F. Lin, Electronic and optical properties of $CsGeX_3$ (X = Cl, Br, and I) compounds, ACS Omega **7**, 25210 (2022).

[69] D. W. Davies, C. N. Savory, J. M. Frost, D. O. Scanlon, B. J. Morgan, and A. Walsh, Descriptors for electron and hole charge carriers in metal oxides, J. Phys. Chem. Lett. **11**, 438 (2020).

[70] R. D. Shannon, Revised effective ionic radii and systematic studies of interatomic distances in halides and chalcogenides, Acta Crys. A **32**, 751 (1976).

[71] Z. Deng, Y. Mo, and S. P. Ong, Computational studies of solid-state alkali conduction in rechargeable alkali-ion batteries, NPG Asia Mater. **8**, e254 (2016).

[72] R. Murugan, V. Thangadurai, and W. Weppner, Fast lithium ion conduction in garnet-type $Li_7La_3Zr_2O_{12}$, Angew. Chem. Int. Ed. **46**, 7778 (2007).

[73] J.-P. Correa-Baena, M. Saliba, T. Buonassisi, M. Grätzel, A. Abate, W. Tress, and A. Hagfeldt, Promises and challenges of perovskite solar cells, Science **358**, 739 (2017).

[74] M. Bag, L. A. Renna, R. Y. Adhikari, S. Karak, F. Liu, P. M. Lahti, T. P. Russell, M. T. Tuominen, and D. Venkataraman, Kinetics of ion transport in perovskite active layers and its implications for active layer stability, J. Am. Chem. Soc. **137**, 13130 (2015).

[75] J. M. Azpiroz, E. Mosconi, J. Bisquert, and F. De Angelis, Defect migration in methylammonium lead iodide and its role in perovskite solar cell operation, Energy Environ. Sci. **8**, 2118 (2015).

[76] C. Eames, J. M. Frost, P. R. F. Barnes, B. C. O'Regan, A. Walsh, and M. S. Islam, Ionic transport in hybrid lead iodide perovskite solar cells, Nat. Commun. **6**, 7497 (2015).

[77] K. Eggestad, B. A. D. Williamson, D. Meier, and S. M. Selbach, Mobile intrinsic point defects for conductive neutral domain walls in $LiNbO_3$, J. Mater. Chem. C **12**, 17099 (2024).

[78] Y. Wang, C. Nelson, A. Melville, B. Winchester, S. Shang, Z.-K. Liu, D. G. Schlom, X. Pan, and L.-Q. Chen, $BiFeO_3$ domain wall energies and structures: A combined experimental and density functional theory+**U** study, Phys. Rev. Lett. **110**, 267601 (2013).

[79] B. Meyer and D. Vanderbilt, *Ab initio* study of ferroelectric domain walls in $PbTiO_3$, Phys. Rev. B **65**, 104111 (2002).

[80] H.-C. Thong, X. Wang, J. Han, L. Zhang, B. Li, K. Wang, and B. Xu, Machine learning interatomic potential for molecular dynamics simulation of the ferroelectric $KNbO_3$ perovskite, Phys. Rev. B **107**, 014101 (2023).

[81] M. Taherinejad, D. Vanderbilt, P. Marton, V. Stepkova, and J. Hlinka, Bloch-type domain walls in rhombohedral $BaTiO_3$, Phys. Rev. B **86**, 155138 (2012).

[82] S. Liu, F. Zheng, N. Z. Koocher, H. Takenaka, F. Wang, and A. M. Rappe, Ferroelectric domain wall induced band-gap reduction and charge separation in organometal halide perovskites, J. Phys. Chem. Lett. **6**, 693 (2015).

[83] D. R. Småbråten, T. S. Holstad, D. M. Evans, Z. Yan, E. Bourret, D. Meier, and S. M. Selbach, Domain wall mobility and roughening in doped ferroelectric hexagonal manganites, Phys. Rev. Res. **2**, 033159 (2020).

[84] G. Stone, D. Lee, H. Xu, S. R. Phillpot, and V. Dierolf, Local probing of the interaction between intrinsic defects and ferroelectric domain walls in lithium niobate, Appl. Phys. Lett. **102**, 042905 (2013).

[85] S. H. Skjærvø, D. R. Småbråten, N. A. Spaldin, T. Tybell, and S. M. Selbach, Oxygen vacancies in the bulk and at neutral domain walls in hexagonal $YMnO_3$, Phys. Rev. B **98**, 184102 (2018).

[86] Y. Kumagai and N. A. Spaldin, Structural domain walls in polar hexagonal manganites, Nat. Commun. **4**, 1540 (2013).

[87] D.-K. Seo, N. Gupta, M.-H. Whangbo, H. Hillebrecht, and G. Thiele, Pressure-induced changes in the structure and band gap of $CsGeX_3$ (X = Cl, Br) studied by electronic band structure calculations, Inorg. Chem. **37**, 407 (1998).

[88] K. Eggestad, B. A. D. Williamson, and S. M. Selbach, $CsGeX_3$ (X = Cl, Br, I) Structure files, Zenodo, 2025, doi: 10.5281/zenodo.17579570.